3D-SIMULATION OF LUNAR MEGAREGOLITH EVOLUTION: QUANTITATIVE CONSTRAINTS ON SPATIAL VARIATION AND SIZE OF FRAGMENT. T. Liu[1], K. Wünnemann[1,2] and G. Michael[2], [1]Museum für Naturkunde, Leibniz Institute for Evolution and Biodiversity Science, 10115 Berlin, Germany (tiantian.liu@mfn.berlin), [2]Freie Universität Berlin, Malteserstr., 74-100, 12249 Berlin, Germany.

Introduction: The lunar crust was damaged by the intensive impact bombardment. It caused a layer consisting of different-sized fragments known as megaregolith [1]. Understanding the evolution of megaregolith can shed light on the lunar thermal evolution history and help to estimate the lunar overall composition [2]. Previous estimates of megaregolith distribution vary significantly with respect to the vertical extent and the size-frequency distribution of fragments was rarely studied [3-5]. To investigate the structure of megaregolith and its fragment size distribution, we built a spatially resolved numerical model to simulate the process of cumulative impact fragmentation.

Methods: Previously we developed an impact mixing model to trace the evolution of different target components with long-term bombardment [6]. For this study we expanded our model to account for the consequences of cumulative impact fragmentation. We consider craters larger than 20 km and the size-frequency distribution of generated craters follows the Neukum Production Function [7]. We take thirty large-scale basin events into account and treat them separately according to a table of actual lunar basins [8]. The model starts (t_0) slightly earlier than the estimated formation time of the ancient South Pole–Aitken basin (SPA) and ends after the occurrence of the youngest basin (3.8 Ga, Orientale [9]). In total we compute the consequences of 18767 impact events.

We assume an initially pristine lunar crust at t_0. Each impact event damages the crust surrounding the impact site and generates different-sized fragments. Fragmented materials are partially expelled from the crater forming an ejecta layer in the vicinity of the crater (**allochthonous fragments**) and partially displaced and remain below the crater (par-**autochthonous fragments**). Both allochthonous and par-autochthonous fragments are assumed to be spherical. In addition, we assume that megaregolith is mostly characterized by large fragments and, thus, consider only fragments >1 m in diameter.

Allochthonous fragments. A commonly used power-law relationship is applied to fit the fragment size-frequency distribution of ejected fragments: $N(m) = C_1 m^{-b}$, where $N(m)$ is the cumulative number of fragments with mass $\geq m$, C_1 is a constant and the exponent b is taken to be 1.2 [9, 10]. Larger fragments occur closer to the crater rim [9], and the size of the largest fragments is related to the crater diameter (D): $l_{E0} = C_2 D^{2/3}$, where C_2 is a constant and is taken to be 0.1 [9].

The distribution of ejecta thickness follows a power law [11]: $H(r) = 0.033 R_t (r/R_t)^{-3}$, where r is the distance from the crater center, and $R_t = D_t/2$ is the radius of transient crater. To simulate fragment distribution in ejecta, while ensuring the general thickness distribution, we assume large fragments are located close to the rim and smaller fragments dominate the distal deposit. Although ejecta at any given range are a mixture of different-sized rocks, the decreasing average fragment size with the increasing distance from the crater center has been verified in numerous impact experiments [12] and is in line with field observations.

Par-Autochthonous fragments. The size of par-autochthonous fragments (l_B) is increasing with the distance from the crater floor (r_B). Using a linear relationship between l_B and r_B [13], we determine $l_B = l_{B0} + C_3 r_B$, where l_{B0} is the size of par-autochthonous fragments close to the crater floor and is line with the assumed fragment size according to the acoustic fluidization (AF) model [14]; C_3 is constant and taken to be 0.4 [13].

Later impact events occur on the fractured target and break the fragments into smaller pieces. Their excavated fragments are further smashed and the produced allochthonous fragments follow the $N(m)$ distribution. The fragments underneath the impact site can also be further broken up by the process of par-autochthonous fragmentation. In this model, we consider this to happen if the determined l_B of a certain depth is smaller than the size of exiting fragments.

Distribution of megaregolith: To indicate the general degree of fragmentation, we calculate the volume-weighted average fragment size (l_V) over the surface, where the smaller values indicate the more abundant small fragments.

Vertical structure. The megaregolith displays distinct layering (Figure 1a): an upper megaregolith that mainly consists of ejected fragments with smaller sizes and a thickness of ~2.5 km; a lower megaregolith that mainly contains par-autochthonous fragments beyond 10 km depth. In between, there is no distinct boundary but a transition zone with a thickness of >5 km where allochthonous and par-autochthonous fragments are mixed. The seismic profiling of the lunar crust reveals

an increase of the p-wave velocity with depth which is in line with our predicted vertical structure [15].

As shown in Figure 2b, in the upper megaregolith, ~85% fragments by volume are in meter-scale. In the lower megaregolith, the disturbed deep crust consists of large-scale fragments, and >80% are in kilometer-scale. In the transition zone, ~40% fragments are in kilometer-scale, and the fractions of fragments in the tens of meter- and hundreds of meter-scale are comparable.

Spatial variation. At 4.3 Ga, soon after the SPA event, the lunar surface was covered with a layer of fractured rocks ejected upon the formation of SPA. Large fragments were distributed inside and near the SPA rim while distal regions were covered with smaller debris. Subsequent impacts that could not penetrate to the underlying less-damaged crust comminuted the fragments produced by the SPA impact, enriching the small fragments in the near-surface. After all the basins were formed at 3.8 Ga (Figure 2), due to the stochastic nature of the impacts, the megaregolith displays substantial lateral variability. The initial structure of megaregolith caused by the SPA impact is still evident after 0.5 Ga of intensive bombardment, indicating the essential role of the SPA impact on the lunar geology.

Evolution of megaregolith: We study the model sensitivities by varying settings of fragment distribution. The results illustrate that, although the potential uncertainties of the applied scaling laws could slightly affect the regional distribution of fragment size, the basin-forming events, as the main drivers of the megaregolith formation, control the evolution of megaregolith. With a given list of basin-forming events, especially those formed after the SPA basin, the distribution of megaregolith is generally unaltered. As shown in Figure 1b, the largest SPA-forming event at ~4.3 Ga caused a great volume of fragments. The ejected fragments formed a kilometer-thick clastic layer, and below its cavity, the crust was fractured to a depth greater than tens of kilometers. In the next 0.2 Ga, the occurrence of multiple basin-forming events shattered more pristine crust. Their ejected fragments covered the SPA fragments thickening the layer of highly fractured fragments in the near-surface. Beneath their occurrence region, the par-autochthonous fragmentation process crushed the crust to greater depths. At 3.9 Ga, when most of the basin-forming events had occurred, the global structure of the megaregolith was established. The late-forming Imbrium and Orientale basins excavated deeper, less damaged crust and emplaced large fragments on the surface, which actually reduced the statistical fragmentation degree of the near-surface.

Conclusions: Our modeling results show that megaregolith spatially varies and the fragment size in the top 2 km is four orders of magnitude smaller than that deeper than 10 km. Basin-forming events controlled the megaregolith growth where the SPA impact shaped its structure.

Acknowledgments: This work was supported by German Research Foundation (DFG) CRC TRR 170, subproject A4.

References: [1] Hartmann W. K. and Morbidelli A. (2020) *MPS*, *55*(11), 2472 – 2492. [2] Warren P. H. and Rasmussen K. L. (1987) *J. Geophys. Res. Solid Earth 92*, 3453–3465. [3] McGetchin T. R. et al. (1973) *EPSL*, *20*(2), 226 – 236. [4] Blanchette-Guertin J.-Fe et al. (2012) *JGR: Planets*, *117*(E6). [5] Thompson T. W. et al. (2009) *Geology*, *37*(7), 655 – 658. [6] Liu T. et al. (2020) *Icarus, 339*. [7] Neukum G. (1983) *Univ. of Munich*, 1 – 186. [8] Orgel C. et al. (2018) *JGR: Planets*, *123*(3), 748 – 762. [9] Bart G. D. and Melosh H. J. (2010) *Icarus, 209*(2), 337 – 357. [10] Buhl E. et al. (2014) *Icarus*, *237*, 131 – 142. [11] Pike R. J. (1974) *EPSL*, *23*(3), 265 – 271. [12] Melosh H. J. (1989) *New York: Oxford University*. [13] Kenkmann T. et al. (2006), *37th LPSC*, #1540. [14] Wünnemann K. and Ivanov B. A. (2003) *PSS*, *51*(13), 831 – 845. [15] Hörz F. et al. (1991), *Lunar Sourcebook*, 61 – 120.

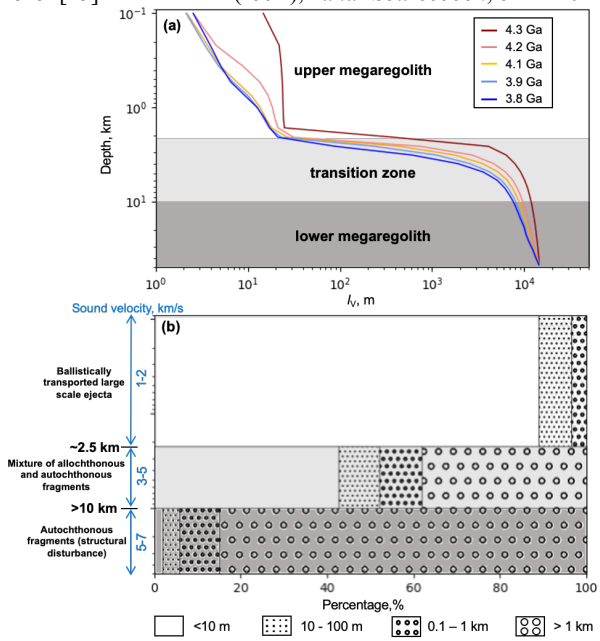

Figure 1. Statistical vertical structure (a) and its fragment size distribution (b) of megaregolith.

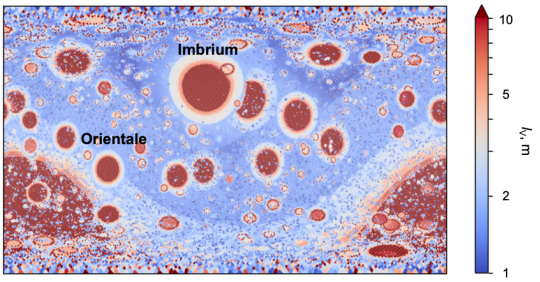

Figure 2. Spatial variation of fragment size over the lunar surface (the top 2 km).